

## 1. Julia family

There is an intriguing possibility that one of the craters on the surface of (89) Julia is directly related to the observed Julia family. In the following, we try to falsify this null-hypothesis, discussing basic properties of the family, and using N-body orbital model, Monte-Carlo collisional model, or SPH collisional model.

### 1.1. Basic observed properties

Regarding the context, Julia family is located in the main belt, but at high inclinations where a low number density of asteroids is expected. At the same time, it is close to the 3/1 mean-motion resonance with Jupiter (see Figure 1). Additionally, there are several secular resonances between J3/1 separatrix and Julia family (2.51 and 2.53 au).

Julia family was already reported in Nesvorný et al. (2015). The family was extracted by a standard procedure, using the hierarchical clustering method (HCM; Zappalà et al. 1995) and a recent catalogue of synthetic proper elements (Knežević & Milani 2003), version Jun 2017. The cutoff velocity  $v_{\text{cut}}$  is treated as a free parameter as it should correspond to *local* conditions, i.e. low background in our case. The number of family members  $N_{\text{fam}}$  depends on  $v_{\text{cum}}$  and this dependence turns out to be flat around  $v_{\text{cut}} = 80 \text{ m s}^{-1}$ , which was chosen for the identification. This family has 66 members; it is composed mainly from *small* asteroids ( $D \in (1; 2.5) \text{ km}$ ) and well separated from background.

No additional criteria were used to remove interlopers, even though we checked Wise catalogue (Masiero et al. 2011) for visual geometric albedos  $p_V$ , Sloan SDSS MOC4 catalogue (Ivezić et al. 2002) for colour indices  $a^*$ ,  $i - z$ , or the semimajor axis vs absolute magnitude ( $a_p, H$ ) plot for any outliers, but there are physical data for only a handful asteroids (due to their faintness) and none of the objects is distinct enough to consider it a clear interloper. Using the population at slightly higher inclinations ( $\sin I_p = 0.30$  to  $0.32$ ) as a representative background we can expect at most 1 interloper among family members anyway.

The family in the space of proper semimajor axis  $a_p$ , proper eccentricity  $e_p$ , and proper inclination  $\sin I_p$  is shown in Figure 2. In the ( $a_p, e_p$ ) plane, it looks like an ‘inclined’ structure, somewhat similar to an ellipse, which can be actually expected for an isotropic ejection if the true anomaly  $f$  at the time of impact was close to  $180^\circ$ . The left-hand part is cut at 2.54 au, most likely due to the proximity of J3/1 resonance; the right-hand part seems more scattered in  $e_p$ . Moreover, its overall size is comparable to the escape velocity from (89) Julia,  $v_{\text{esc}} = \sqrt{2GM/R} \doteq 115 \text{ m s}^{-1}$  if we assume the bulk density  $\rho = 4300 \text{ kg m}^{-3}$ . There is a noticeable offset in inclination by 0.002, likely arising from a cratering and ejection of all fragments into an half-space.

The largest remnant (89) Julia is  $(148 \pm 10) \text{ km}$  in diameter, with the geometric albedo  $p_V = 0.184 \pm 0.034$ . The only other member with known albedo is (242057), but with a substantial uncertainty,  $p_V = 0.268 \pm 0.077$ . We thus use the former value for all other family members. The mean colours of 9 members,  $a^* = 0.044 \text{ mag}$ ,  $i - z = 0.103 \text{ mag}$ , confirm their taxonomy belongs to the S-complex. The slope of the size-frequency distribution is relatively high,  $q = -3.9 \pm 0.2$ , which is far from the collisional equilibrium of Dohnanyi (1969). None of the above properties contradicts the relation between (89) Julia and its family.

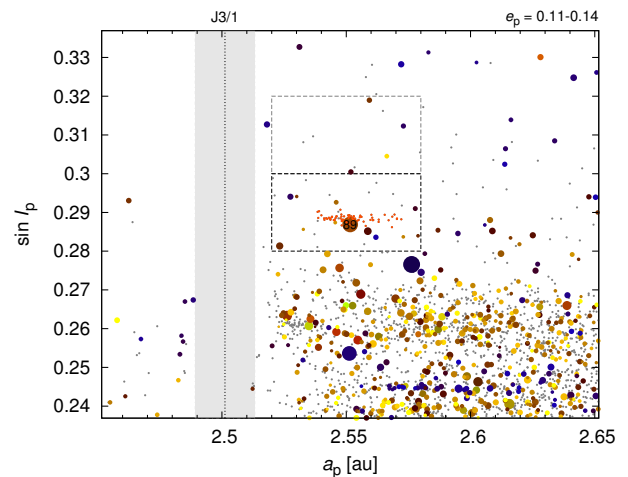


**Fig. 1.** Surroundings of Julia family on the proper semimajor axis  $a_p$  vs proper inclination  $\sin I_p$  plot. All asteroids with eccentricities  $e_p = 0.11$  to  $0.14$  are shown. Symbol sizes are proportional to the logarithm of diameters  $D$ . Colours corresponds to the geometric albedos  $p_V$  (namely  $p_V < 0.07$  is blue,  $p_V > 0.15$  brown and yellow, gray if unknown). The libration centre of the 3/1 mean-motion resonance with Jupiter and its approximate width is denoted by a vertical strip. The black dashed rectangle indicates a region which will be analyzed in detail; the gray one is selected as a suitable background population. The large family at  $\sin I_p < 0.27$  is Maria. The largest asteroid in the neighbourhood is (13) Egeria. Julia family members identified at the cutoff velocity  $v_{\text{cut}} = 80 \text{ m s}^{-1}$  are emphasized by orange colour. The family is composed mainly from small asteroids ( $D \in (1; 2.5) \text{ km}$ ) and well separated from background asteroids.

### 1.2. N-body orbital model

As a first step, we construct an orbital-evolution model. It is based on a symplectic N-body integrator from the Swift package Levison & Duncan (1994), modified according to Laskar & Robutel (2001). This integration scheme makes possible to use the time step  $\Delta t = 91 \text{ d}$  and the time span reaches up to 4 Gyr. Our dynamical model contains perturbations by 4 giant planets (with initial barycentric correction), Yarkovsky diurnal and seasonal effects (Vokrouhlický 1998; Vokrouhlický & Farinella 1999), which induce a systematic drift in  $a$ , but interactions with resonances which may also induce drifts in  $e$ , or  $I$  Brož & Vokrouhlický (2008); the YORP effect with thermal torques from Čapek & Vokrouhlický (2004), corresponding secular evolution of spins, collisional reorientations, mass shedding at a critical spin rate, as outlined in Brož et al. (2011).

For an appropriate comparison with observations, we use online digital filters. To compute mean elements, we perform sampling 1 yr and use convolution filters A, A, A, B from Quinn et al. (1991), with decimation factors 10, 10, 5, 3. Proper elements are computed by the frequency-modified Fourier transform (Šidlichovský & Nesvorný 1996), from 512 samples; planetary frequencies (forced oscillations) are removed to obtain required amplitudes of free oscillations. Finally, we use a running window up to 10 Myr to suppress remaining oscillations due to long-period secular resonances. This averaging involves certain amount of data and delays the initial output (by about 5 kyr for the mean-element filter, 0.8 Myr for the proper-element filter, and 10 Myr for the running window).

Initial conditions of planets were taken from DE405 ephemeris, and osculating elements of asteroids from Astorb catalogue. All planets and (89) Julia were integrated from the epoch of osculation until the true anomaly reached  $f = 180^\circ$

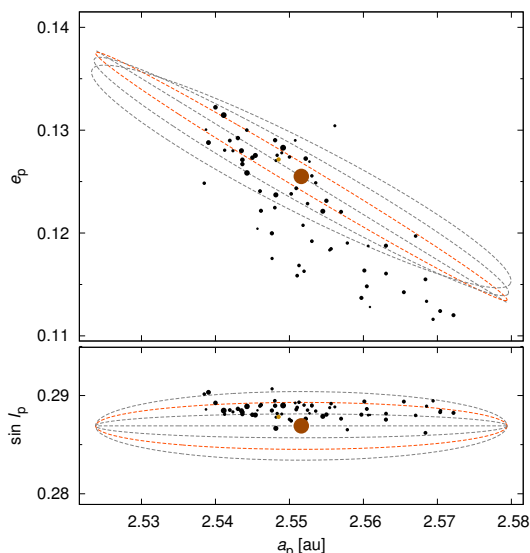


**Fig. 2.** Julia family in the space of proper elements ( $a_p$ ,  $e_p$ ,  $\sin I_p$ ), as extracted by the hierarchical clustering method (HCM) with the cutoff velocity  $v_{\text{cut}} = 80 \text{ m s}^{-1}$ . The ellipses correspond to a constant velocity difference with respect to (89) Julia, equal to the escape velocity  $v_{\text{esc}} \doteq 115 \text{ m s}^{-1}$  from the respective parent body. Their shape is determined by the Gauss equations, the true anomaly  $f$ , and the argument of perihelion  $\omega$  at the time of breakup. In particular, we show the values  $f = 180^\circ, 170^\circ, 160^\circ, 150^\circ$  (top panel);  $f + \omega = 90^\circ, 80^\circ, 70^\circ$ , and  $60^\circ$  (bottom panel). These ellipses seem to indicate that the relation between (89) Julia and its family is reasonable.

and  $\omega + f = 80^\circ$ . We then generated 660 bodies, i.e. 10 times the observed number in order to get a large sample of orbits, so that it can be easily resampled off-line. For simplicity, we assumed an isotropic velocity field, and a distribution of Farinella et al. (1994), with the slope  $\alpha = 1.25$  and the maximum velocity  $v_{\text{max}} = 500 \text{ m s}^{-1}$  (to get also outliers). This distribution peaks at about the escape velocity  $v_{\text{esc}}$ . We also assumed initially isotropic spins, and a uniform distribution of spin periods,  $P \in (2; 10) \text{ h}$ .

Thermal parameters of synthetic bodies were selected as follows. The bulk density  $\rho = 4300 \text{ kg m}^{-3}$ , the density of surface layers (regolith)  $\rho_{\text{surf}} = 1500 \text{ kg m}^{-3}$ , the heat capacity  $C = 680 \text{ J kg}^{-1} \text{ K}^{-1}$ , the thermal conductivity  $K = 10^{-3} \text{ W m}^{-1} \text{ K}^{-1}$ , the Bond albedo  $A = 0.10$ , and the infrared emissivity  $\epsilon = 0.9$ . Diameters were taken from the observed SFD, with 10 clones for each.

The orbital evolution of the synthetic family is shown in Figure 3 (left column). Qualitatively, it is clear that in about 100 Myr the synthetic family becomes too dispersed compared to the observations. However, we cannot *directly* (quantitatively) compare the outcome of N-body simulations and observations as there are at least three problems (Brož 2016): observed asteroids have to be carefully selected, not only the family identified by HCM, but also its surroundings, where the bodies can be scattered to (cf. Brož & Morbidelli (2013)); the SFD is different and it even changes in the course of the simulation; there is an inevitable contribution of background asteroids, and this background can be even variable.

To overcome these limitations we post-process the output of our N-body simulation. As a preparation, we have to select all observed asteroids which encompass the family, i.e.  $a_p \in (2.52; 2.58) \text{ au}$ ,  $e_p \in (0.11; 0.14)$ ,  $\sin I_p \in (0.28; 0.30)$ , with physical parameters (if known)  $p_V \in (0.07; 0.40)$ ,  $a^* \in$

$(0.0; 0.2) \text{ mag}$ ,  $i - z \in (-0.2; 0.2) \text{ mag}$ , i.e. S-complex taxonomy (or unknown). Suitable background population is almost the same, except  $\sin I_p \in (0.30; 0.32)$  (see the rectangles in Fig. 1).

We then proceed with a so-called ‘black-box’ method (cf. Fig. 3 middle column): (i) we choose 4 boxes with  $\Delta a = 0.03 \text{ au}$ ,  $\Delta e = 0.015$ ; (ii) we compute the numbers of observed asteroids located in these boxes; (iii) the observed differential SFD; (iv) the background differential SFD; (v) at every single output time step we compute the synthetic differential SFD (saving also lists of bodies in the respective bins); (vi) for every single size bin ( $D, D + dD$ ) we draw a synthetic background population from a random uniform distribution (in  $a_p, e_p, \sin I_p$ ), because our volume is relatively small; if the background volume differs from our volume, we have to use a suitable factor  $f$ ; (vii) we *rescale* the synthetic SFD to the observed one by randomly choosing  $N_{\text{obs}} - fN_{\text{bg}}$  bodies from the lists; (viii) we compute the numbers of all synthetic asteroids located in the boxes; (ix) finally, we compute the metric

$$\chi^2 = \sum_{i=1}^{N_{\text{box}}} \frac{(N_{\text{syn}i} - N_{\text{obs}i})^2}{\sigma_{\text{syn}i}^2 + \sigma_{\text{obs}i}^2}, \quad (1)$$

where the uncertainties are assumed Poisson-like,  $\sigma = \sqrt{N}$ . Unfortunately, in our case the family is rather small, so are the numbers of bodies in boxes, and consequently the uncertainties are relatively large. We have to keep in mind that the temporal evolution  $\chi^2(t)$  is somewhat noisy, and sometimes a random selection of bodies may also lead to a good fit. Nevertheless, according to Fig. 3 (right column) it is clear that systematically good fits are only possible for ages  $t \lesssim 100 \text{ Myr}$ , with the best one at  $t = 20 \text{ Myr}$ . The lower limit  $t \gtrsim 10 \text{ Myr}$  stems from the fact that the left-hand part of the family below  $2.54 \text{ au}$  needs to be dispersed. Having these results, the N-body model of Julia family seems to be reasonable.

Let us note, however, that our dynamical model is simplified and may be insufficient. For example, we do not account for massive asteroids (89) Julia, (13) Egeria which may possibly perturb the orbits and create an additional dispersion of the family between  $a_p = 2.55$  to  $2.57 \text{ au}$ . Another possibility is that the velocity field was substantially anisotropic, apart from being shifted wrt. (89) Julia. This may also help to precisely match the observed dispersion in orbital elements.

In order to account for the dynamical decay also in Monte-Carlo collisional models we computed the relative numbers of asteroids  $N(t)/N_0$  located within the respective region (Figure 4). They can be approximated by exponentials,  $N/N_0 = \exp(-t/\tau)$ , and the respective time scales  $\tau$  for five different size bins  $D \in (0.5; 2.5) \text{ km}$ , and  $150 \text{ km}$  to account for the largest remnant, are as follows: 226, 434, 595, 424 Myr (and formally 42 200 Myr, i.e. very long).

### 1.3. Monte-Carlo collisional model

Knowing the orbital evolution, we are ready to construct a collisional model. To this point we use a Monte-Carlo code called Boulder (Morbidelli et al. 2009), which computes the evolution of size-frequency distributions due to fragmentation (and reaccumulation). We only performed a few modifications (as in Cibulková et al. 2014), most importantly we account for a size-dependent dynamical decay (mostly due to the Yarkovsky effect and neighbouring resonances), including a handling of fractional probability.

Hereinafter, we assume two populations: the main belt and Julia family. Because the family is located at the outskirts of the

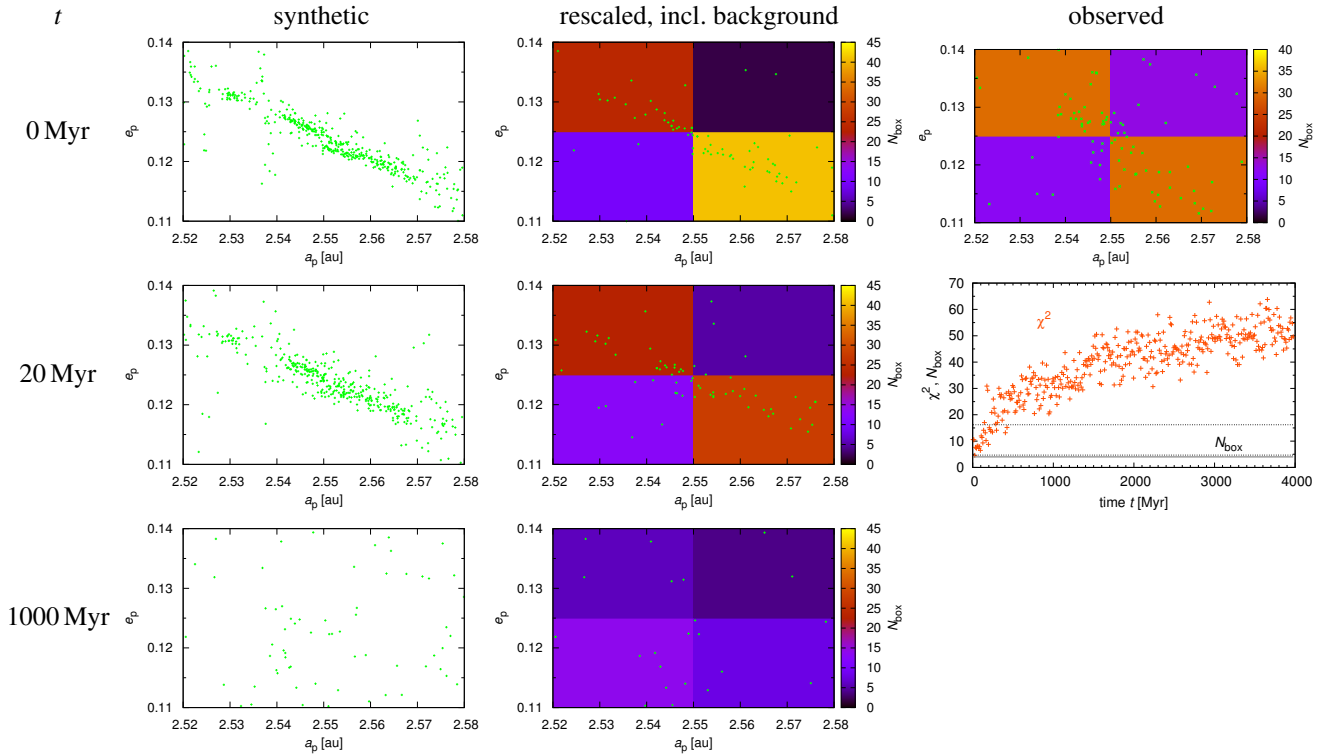


**Fig. 3.** The proper semimajor axis  $a_p$  vs the proper eccentricity  $e_p$  for the synthetic family (left column). It is an output of the N-body simulation which initially included 660 bodies (i.e. 10 times more than observed). It was later rescaled to the same size-frequency distribution (SFD) as the observed one, and we included also a *random* background population (middle column). Colours correspond the numbers of bodies  $N_{\text{box}}$  in the respective boxes. Finally, there is the observed family, and the corresponding  $\chi^2$  metric (right column). The ‘initial’ conditions are shown as  $t = 0$  Myr (top row), as well as the best fit at  $t = 20$  Myr (bottom row). Dotted lines on the  $\chi^2(t)$  plot correspond to the  $1\text{-}\sigma$  and  $3\text{-}\sigma$  levels. A reasonable match is only possible for young ages  $t \lesssim 100$  Myr.

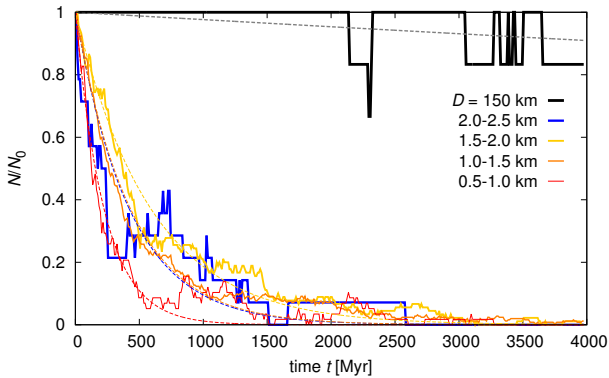


**Fig. 4.** A relative number  $N/N_0$  of the synthetic family members vs time  $t$  (solid lines), for five different size bins spanning  $D \in (0.5; 2.5)$  km, and 150 km to account for the largest remnant. A body is removed from the population whenever it leaves a region in the proper element space outlined by:  $a_p \in (2.52; 2.58)$  au,  $e_p \in (0.11; 0.14)$ ,  $\sin I_p \in (0.28; 0.30)$ . This dynamical decay can be approximated by exponentials (dashed lines),  $N/N_0 = \exp(-t/\tau)$ . The respective time scales  $\tau$  are then used for the Monte-Carlo collisional model.

main belt we computed intrinsic collisional probabilities anew, using the algorithm by Bottke & Greenberg (1993). The actual values are  $P_i = 2.99 \times 10^{-18} \text{ km}^{-2} \text{ yr}^{-1}$  within the main belt,  $3.84 \times 10^{-18} \text{ km}^{-2} \text{ yr}^{-1}$  for mutual collisions, and  $6.10 \times 10^{-18} \text{ km}^{-2} \text{ yr}^{-1}$  within the family (even though these collisions are clearly negligible). The respective median impact velocities are  $v_{\text{imp}} = 5.04, 6.62,$  and  $6.57 \text{ m s}^{-1}$ . Main-belt decay is taken from Bottke et al. (2005), Julia from above.

Physical properties of the populations are described by the scaling law  $Q_D^* = Q_0 r^a + B p r^b$ , where we use the parameters from Benz & Asphaug (1999) for basalt at 5 km/s, with one exception for Julia family for which we use a higher density ( $\rho = 4.3 \text{ g cm}^{-3}$ ) what makes it slightly stronger in the gravity regime.

Initial conditions or SFDs are rather similar to the observations except the tails which were prolonged down to  $D_{\text{min}} = 0.005$  km, or eventually bend-off below slope  $q = -3$  to prevent a divergence in mass. The time step is  $\Delta t = 10$  Myr (or smaller if necessary), the time span up to 4 Gyr. The model has to be run multiple times because of the fractional probabilities.

Results are shown in Figure 5 (left column). It turns out that Julia family is by no means an exception, because collisions with (89) Julia creating such populations are relatively frequent. On the other hand, if we focus on a *single* event (right column), without (89) Julia itself which creates fragments all the time, this transient population decays within a few 100 Myr, partly because of the dynamical decay and partly due to collisional grinding. This young age is consistent with the previous orbital model. Again, we can state that our (statistical) collisional model of Julia family seems reasonable.

#### 1.4. SPH collisional model

Last but not least, we try to use an SPH model, from which we can estimate the ejected mass, size-frequency distribution of fragments, their velocity field, and most importantly, the crater size. All of these may potentially contradict the observations.

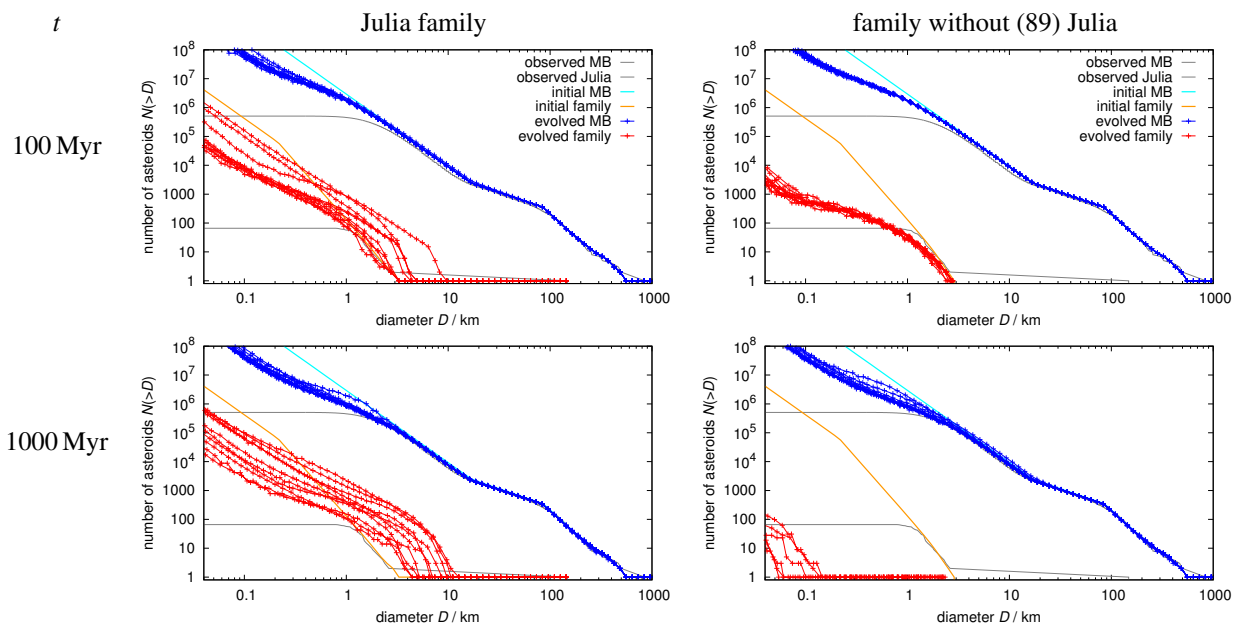


**Fig. 5.** Cumulative size-frequency distributions  $N(>D)$  resulting from two Monte-Carlo collisional models: the main belt and Julia family (left column); the main belt and the family without the largest remnant (89) Julia (right column). The main belt SFD is plotted in blue and the family SFD in red; the respective initial conditions in cyan and yellow, and the observations are in gray; the bend-off at around  $D \simeq 1$  km is mostly due to the observational incompleteness. The situation at time  $t = 100$  Myr (top row), and  $t = 1000$  Myr (bottom row) is shown. There are always 10 runs with a different random seed, in order to see also lower-probability events. The first model demonstrates that Julia family is by *no means* an exception, while the second one that small fragments (from a single breakup) decay quickly within a few 100 Myr at most.

As a preparatory task, we employ a set of Durda et al. (2007) size-frequency distributions and a simple scaling (up to  $D = 150$  km) discussed therein to preliminary estimate impact parameters from the observed SFD (cf. Figure 7). Given the ‘vast’ difference between the largest remnant (i.e. the 1st largest body) and the largest fragment (2nd), it is not surprising that the best-fit SFD corresponds to a smallest cratering at an oblique angle which imparts only a limited amount of energy on to the target. The expected projectile size is thus  $d = 8.117$  km, the velocity  $v_{\text{imp}} = 6$  km s $^{-1}$ , and the angle  $\vartheta_{\text{imp}} = 75^\circ$ .

We use the following tools for computations: SPH5 code for the fragmentation phase (Benz & Asphaug 1994), Pkdgrav for the reaccumulation phase (Richardson et al. 2000), Tillotson (1962) equation of state, von Mises (1913) yielding criterion, and Grady & Kipp (1980) fracture model.

Material parameters mostly correspond to basalt (except  $\rho_0$ ): the zero-pressure density  $\rho_0 = 4.3$  g cm $^{-3}$ , bulk modulus  $A = 2.67 \cdot 10^{11}$  erg cm $^{-3}$ , non-linear compressive term  $B = 2.67 \cdot 10^{11}$  erg cm $^{-3}$ , Tillotson parameters  $E_0 = 4.87 \cdot 10^{12}$  erg g $^{-1}$ ,  $a = 0.5$ ,  $b = 1.5$ ,  $\alpha = 5.0$ , and  $\beta = 5.0$ , incipient vaporization  $E_{\text{iv}} = 4.72 \cdot 10^{10}$  erg g $^{-1}$ , complete vaporization  $E_{\text{cv}} = 1.82 \cdot 10^{11}$  erg g $^{-1}$ , shear modulus  $\mu = 2.27 \cdot 10^{11}$  erg cm $^{-3}$ , yielding  $Y = 3.5 \cdot 10^{10}$  erg g $^{-1}$ , melt energy  $E_{\text{melt}} = 3.4 \cdot 10^{10}$  erg g $^{-1}$ , tensile failure using Weibull flaws, with fracture parameters  $k = 4.0 \cdot 10^{29}$  cm $^{-3}$ , and  $m = 9.0$ .

The time step  $\Delta t$  is controlled the Courant criterion with a factor 1.0. The time span 100 s is more than twice longer than the travel time of the shock wave,  $2D/v_{\text{imp}}$ , and much shorter than the ejection time scale,  $v_{\text{ej}}/g$ . Artificial viscosity parameters were set a bit higher than standard ones,  $\alpha_{\text{av}} = 4.0$ ,  $\beta_{\text{av}} = 8.0$ . We use a modification of the scalar damage  $\mathcal{D}$  as explained in Ševeček et al. (2017) (App. C). The number of SPH particles was  $N_{\text{part}} \simeq 7.0 \times 10^5$ .

The handoff, or conversion of SPH particles to solid spheres, was performed with the relation  $R_i = [3m_i/(4\pi\rho_i)]^{1/3}$ , which

allows for some expansion below  $\rho_0$ . In the reaccumulation phase, the self-gravity was computed approximately, with gravitational moments up to hexadecapole order and the opening angle  $\theta = 0.5$  rad. We assumed a perfect merging, so that no shape information is preserved. The time step was  $10^{-6}$  (in  $G = 1$  units) and the time span  $50\,000\Delta t$  so that the reaccumulation is definitively over.

Before we proceed with the discussion of the crater visible in Figure 6, we have to check the resulting size-frequency distribution (after the reaccumulation) which is plotted in Figure 7. The largest fragment (2nd) is resolved and matches quite well the observations, even though its size is a bit larger (3 vs 2 km). The remainder of the SFD cannot be directly compared thought, because its slope is driven by the limited resolution; the sizes of individual (not reaccumulated) particles differ only due their expansion during the fragmentation phase. Nevertheless, we can retain the original impact parameters and also the resolution, because our model SFD does not contradict the observations.

Regarding the crater, we should estimate its final size, e.g. rim-to-rim, but we only have a transient crater at the end of the fragmentation phase. To overcome this issue, we overplotted distances  $s$  which would be travelled by particles within a ballistic time  $t = 2v \sin 45^\circ/g$  at a given (approximately homogeneous) gravity  $g = GM/R^2$ . If  $s < h$ ,  $h$  denoting the smoothing length, the particle cannot travel anyway far from its current position. Consequently, if we carefully measure Fig. 6, the diameter of the resulting crater should be at least  $d_{\text{crater}} \geq 60$  km, but this is still transient (it can become larger due to later landslides) and without the ejecta blanket, of course. This value seems in a striking agreement with the observed sizes of the four craters (ranging from ??? to ??? km).

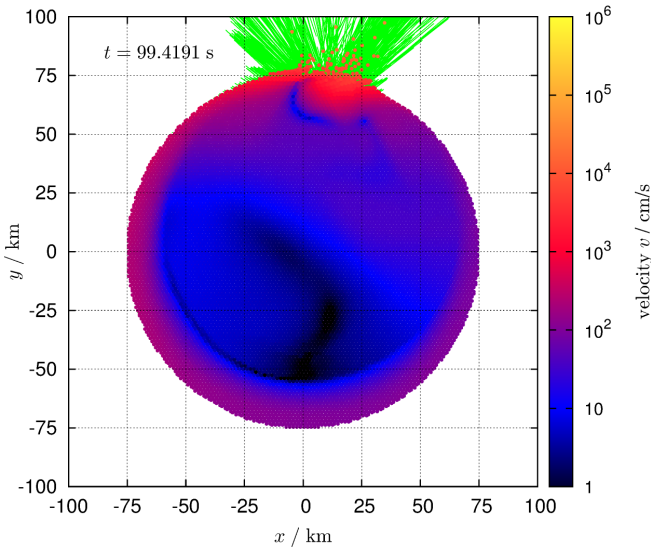


**Fig. 6.** An SPH model of the breakup of a  $D = 150$  km target. Its cross-section in  $(x, y)$  plane is shown, with colours corresponding to the logarithm of velocity  $|v|$ . The number of SPH particles used was  $N_{\text{part}} \approx 7.0 \times 10^5$ . The time  $t \approx 100$  s corresponds to the end of fragmentation phase. (The reaccumulation phase is computed later by an N-body model with self-gravity.) The original projectile had size  $d = 8.117$  km, velocity  $v_{\text{imp}} = 6$  km  $\text{s}^{-1}$ , and hit the target at a very oblique angle  $\vartheta_{\text{imp}} = 75^\circ$ . Green lines indicate the distances  $s$  which would be travelled by particles within a ballistic time  $t = 2v \sin 45^\circ / g$  at a given (approximately homogeneous) gravity  $g = GM/R^2$ . Consequently, the diameter of the resulting (transient) crater should be at least  $d_{\text{crater}} \approx 60$  km.

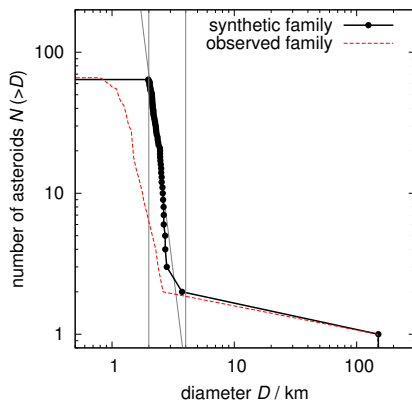


**Fig. 7.** The cumulative size-frequency distribution resulting from the SPH plus N-body simulation of the breakup (black solid line), compared to the observed SFD of Julia family (red dashed line). Fast-moving projectile fragments were removed from the plot as they can never be associated with the family. The largest remnant (i.e. the 1st largest body) remains practically the same; the largest fragment (2nd) is already resolved, even though its size is a bit larger than the observations (3 vs 2 km). The remainder of the SFD cannot be directly compared, because its slope is driven by the limited resolution; the sizes of individual (not reaccumulated) particles differ only due their expansion during the fragmentation phase.

### 1.5. Ejecta half-space position

We can further analyze the velocity field resulting from the SPH model. As expected for a cratering event, ejecta can only fly to an half-space, and there is a significant shift between the largest remnant and remaining fragments (although we remind they are not fully resolved). Ejection velocity with respect to the barycen-

ter (without outliers like projectile fragments) is of the order of  $v_{\text{ej}} \approx 100$  m  $\text{s}^{-1}$ . Using Gauss equations, this translates to a shift in  $\Delta I = \Delta v_W / (na \sqrt{1 - e^2}) r / a \cos(\omega + f) \approx 0.002$  rad for a suitable orientation of the ejection half-space, i.e. just above the orbital plane. This is indeed comparable to the difference observed for Julia family (as discussed in Sec. 1.1).

Because the orbital angular momentum  $L_{\text{orb}}$  of the projectile is only about 1/10 of the rotational angular momentum  $L_{\text{rot}}$  of the target, we can also assume that even the most oblique impacts cannot ‘flip’ the rotation axis. This actually allows us to identify, or at least try to, which of the four craters is the one related to Julia family.

Given the known orientation of the spin axis and the orientation of the orbit, the obliquity of (89) Julia is  $\gamma = -17^\circ$ . It means that latitude  $\phi = \gamma$  is the one at which ejecta can fly mostly above the orbital plane (in  $W$  direction). Because the centres of the three northern-hemisphere craters are located at about  $\phi \approx +30^\circ$ , i.e. offset by almost  $50^\circ$ , we can prefer the southern-hemisphere crater as the origin of Julia family.

Of course, we cannot exclude a possibility that the situation is more complicated, e.g. by very anisotropic velocity fields, two (or more) overlapping families, material properties different from what we assumed, etc. We also admit the northern-hemisphere craters are simply more numerous and more probable (3/4) from the statistical point of view.

## 2. Conclusions

Using a detailed study of Julia family, we were *not* able to rule out a hypothesis that one of the craters is related to Julia family. On contrary, all three models (N-body, Monte-Carlo and SPH) and their mutual consistency indicate that fragments ejected from (89) Julia indeed formed a family, 10 to 100 Myr ago. We can even prefer one crater (out of four), because it is located on the southern hemisphere which seems more suitably oriented with respect to the family. For the first time, we were able to suggest such a link solely on the basis of ground-based observations. It may be considered a beginning of a new era of asteroid-family studies, which shall include families  $\leftrightarrow$  craters identifications.

## References

- Benz, W. & Asphaug, E. 1994, *Icarus*, 107, 98
- Benz, W. & Asphaug, E. 1999, *Icarus*, 142, 5
- Bottke, W. F., Durda, D. D., Nesvorný, D., et al. 2005, *Icarus*, 179, 63
- Bottke, W. F. & Greenberg, R. 1993, *Geophys. Res. Lett.*, 20, 879
- Brož, M. 2016, in AAS/Division for Planetary Sciences Meeting Abstracts, Vol. 48, AAS/Division for Planetary Sciences Meeting Abstracts #48, 400.03
- Brož, M. & Morbidelli, A. 2013, *Icarus*, 223, 844
- Brož, M. & Vokrouhlický, D. 2008, *MNRAS*, 390, 715
- Brož, M., Vokrouhlický, D., Morbidelli, A., Nesvorný, D., & Bottke, W. F. 2011, *MNRAS*, 414, 2716
- Cibulková, H., Brož, M., & Benavidez, P. G. 2014, *Icarus*, 241, 358
- Dohnanyi, J. S. 1969, *J. Geophys. Res.*, 74, 2531
- Durda, D. D., Bottke, W. F., Nesvorný, D., et al. 2007, *Icarus*, 186, 498
- Farinella, P., Froeschle, C., & Gonczi, R. 1994, in IAU Symposium, Vol. 160, Asteroids, Comets, Meteors 1993, ed. A. Milani, M. di Martino, & A. Cellino, 205
- Grady, D. & Kipp, M. 1980, *International Journal of Rock Mechanics and Mining Sciences & Geomechanics Abstracts*, 17, 147
- Ivezić, Ž., Lupton, R. H., Jurić, M., et al. 2002, *AJ*, 124, 2943
- Knežević, Z. & Milani, A. 2003, *A&A*, 403, 1165
- Laskar, J. & Robutel, P. 2001, *Celestial Mechanics and Dynamical Astronomy*, 80, 39
- Levison, H. F. & Duncan, M. J. 1994, *Icarus*, 108, 18
- Masiero, J. R., Mainzer, A. K., Grav, T., et al. 2011, *ApJ*, 741, 68

- Morbidelli, A., Bottke, W. F., Nesvorný, D., & Levison, H. F. 2009, *Icarus*, 204, 558
- Nesvorný, D., Brož, M., & Carruba, V. 2015, *Identification and Dynamical Properties of Asteroid Families*, ed. P. Michel, F. E. DeMeo, & W. F. Bottke, 297–321
- Quinn, T. R., Tremaine, S., & Duncan, M. 1991, *AJ*, 101, 2287
- Richardson, D. C., Quinn, T., Stadel, J., & Lake, G. 2000, *Icarus*, 143, 45
- Tillotson, J. H. 1962, *General Atomic Report GA-3216*
- Čapek, D. & Vokrouhlický, D. 2004, *Icarus*, 172, 526
- Ševeček, P., Brož, M., Nesvorný, D., et al. 2017, *Icarus*, 296, 239
- Šidlichovský, M. & Nesvorný, D. 1996, *Celestial Mechanics and Dynamical Astronomy*, 65, 137
- Vokrouhlický, D. 1998, *A&A*, 335, 1093
- Vokrouhlický, D. & Farinella, P. 1999, *AJ*, 118, 3049
- von Mises, R. 1913, *Nachrichten von der Gesellschaft der Wissenschaften zu Göttingen, Mathematisch-Physikalische Klasse*, 582
- Zappalà, V., Bendjoya, P., Cellino, A., Farinella, P., & Froeschlé, C. 1995, *Icarus*, 116, 291